Gravity sparse inversion using the interior-point method and a general model weighting function

WENWU ZHU[1,2], JUNHUAN PENG[2,3,✉], SANMING LUO[1], XIANGANG MENG[1], JINZHAO LIU[1] AND CHUANDONG ZHU[1]

1 First Crust Monitoring and Application Center, CEA, Tianjin 300180, China

2 China University of Geosciences, Beijing 100083, China (375138766@qq.com)

3 Shanxi Key Laboratory of Resources, Environment and Disaster Monitoring CN, Shanxi 030006, China

Received: April 17, 2020; Revised: July 2, 2020; Accepted: August 18, 2020

ABSTRACT

This study presents an optimized gravity-sparse inversion method. The proposed method minimizes the global objective function using interior-point method for boundary constraints and a general weighting function comprising the depth, compactness, and kernel weighting functions of the density models. For the compactness weighting function, practical experiments demonstrate that the recovered model becomes more compact with an increasing value for the relative exponential factor β. However, if no appropriate boundary-constraint method is applied, the inversion results cannot be controlled within the designated constraint bounds when β needs to be set to a large value to obtain compact inversion results. The interior-point method allows the use of a larger β to obtain more compact inversion results without violating the boundary constraints. Additionally, models in close proximity can more clearly be recognized using this method. To improve the computational efficiency and obtain a more accurate regularization parameter, the preconditioned conjugate gradient and L-curve, or line search methods, were also applied. The proposed method was applied for three synthetic examples: two positive bodies adjacent to each other at different depths inverted using noise-free gravity anomaly data, three bodies (positive or negative) at different depths inverted using noise-free or contaminated gravity anomaly data, and three bodies (positive or negative) characterized by a certain dip angle inverted using contaminated gravity anomaly data. This method was also applied for the inversion of a Woodlawn sulfide body, Missouri iron ore body, and granitoid rock body in the Rio Maria region in the state of Para, Brazil. In all six test cases, larger β values were used and the density models were recovered with sharper boundaries within the designated bounds.

Keywords: gravity anomalies, Earth structure, geophysical methods, inverse theory, geodesy

1. INTRODUCTION

Gravity and magnetic inversions are inexpensive methods that have been extensively applied in the fields of hydrology, geological surveys, oil and gas exploration, mineral exploration, and earthquake prediction (*Mendoca and Silva, 1994, 1995*; *Blakely, 1995*; *Li and Oldenburg, 1996, 1998*; *Pilkington, 1997*; *Portniaguine and Zhdanov, 1999*; *Chen et al., 2008*; *Zhdanov, 2015*). Discretization of the Earth model into several grids is typically an essential step when using a computer to perform inversion investigations. The design of this model discretization can be divided into two types. The first type uses variable values inside each model element while the second type uses model elements that are constant. However, due to the instability and non-uniqueness of the inversion, referred to as "an ill-posed problem" (*Hadamard, 1902*), obtaining accurate inversion information in accordance with the real Earth model is difficult. The regularization theory proposed by *Tikhonov (1943)* and *Tikhonov and Arsenin (1977)* allows a solution to this ill-posed problem. With this theory, previous studies have extensively examined implementations of weighting the data and model. In addition, the regularization parameter is typically obtained using the L-curve method (*Hansen and O'Leary, 1993*; *Hansen, 1994*).

Different weighting functions yield different inversion solutions. There are two types of weights to consider: (1) the weight of the data in the inversion calculation, which can be represented by estimating the variance of the observations (*Zhdanov, 2015*) and (2) the weight of the model. *Li and Oldenburg (1996, 1998)* used an inverse function of the depth, known as the depth weighting function, to counteract the well-known problem of concentration near the surface due to ambiguity or non-uniqueness. Another type of weighting function, known as kernel weighting, which is only related to the kernel matrix, was proposed by *Mendonca and Silva (1994, 1995)*, *Stocco et al. (2009)*, *Zhdanov (2015)* and *Ghalehnoee et al. (2017)*. To obtain compact inversion results, a third type of weighting, known as the compactness weighting function, has been defined via the iteratively reweighted least squares (IRLS) method (*Last and Kubik, 1983*). As the iteration algorithm deepens, the inversion values of certain blocks concentrate at the upper or lower bounds while most other values approach zero. *Portniaguine and Zhdanov (1999)* improved this method by adding a reference model in the compactness weighting function based on the "minimum structure" principle. *Ghalehnoee et al. (2017)* and *Rosas-Carbajal et al. (2017)* introduced a general weighting function composed of depth weighting, kernel weighting, and compactness weighting functions.

Even if a general weighting function is used in the regularization method, accurate inversion results are still insufficient, where additional prior information must be added to implement more constraints on the regularization object function. Among these approaches, previous studies commonly define boundary constraints based on practical experience. In general, model density values cannot be less than zero, such that positivity constraints ensure that the inversion model is greater than zero (*Li and Oldenburg, 1996, 2003*; *Pilkington, 1997, 2009*). If the upper and lower bounds of the density have been established in the research field, the upper and lower boundary constraints should be applied at the same time in the inversion process. One method for enforcing boundary constraints is to freeze model blocks that cross the bounds by applying relatively large weights (i.e., 10^{10} to replace ∞) on the blocks in the subsequent iterative process (*Last and*

Kubik, 1983; *Guillen and Menichetti, 1984*). The relative exponential factor β of the compactness weight refers to the use of the L_p norm (*Sun and Li, 2014*). When $\beta = 2$, the L_0 norm is used; however, if $\beta = 1$ or $\beta = 0$, then the L_1 or L_2 norms, respectively, are used. Furthermore, β cannot be set arbitrarily; if it is too small, the recovered model will not have sharp boundaries but if it is too large, the inversion results will typically not be constrained within the designated scope. These two phenomena were observed in a study conducted by *Ghalehnoee et al. (2017)*. Based on the previously mentioned problem, the interior-point constraint method has been adopted to allow a slightly higher β to obtain sharper boundaries within the specified bounds (*Li and Oldenburg, 2003*).

This study focuses on the problem of a recovered model exceeding the designated bounds for large values of β. We propose a gravity inversion using the interior-point method with a general model weighting function to produce a more compact recovered model without exceeding the designated bounds. First, we discuss the regularization algorithm using the interior-point method supported by the one-step Newton method and the preconditioned conjugate gradient method (*Pilkington, 1997*; *Li and Oldenburg, 2003*; *Li et al., 2018*). We also improve the interior-point algorithm in which zero occasionally appears in the denominator. Next, we discuss the general weighting function of the model used in the inversion process. We then apply the combined method to synthetic and field examples, comparing the inversion results to those reported in *Ghalehnoee et al. (2017)*.

2. MATERIALS AND METHODS

The density model was assumed to be discretized into a number of rectangles in two-dimensional (2-D) models or rectangular prisms in three-dimensional (3-D) models. For simplicity, the inversion method was introduced for a 2-D case in this example, but the discussion equally applies to the 3-D case. The gravity anomaly data, $\boldsymbol{d}$, has the following relationship with the density model, $\boldsymbol{m}$:

$$\boldsymbol{d} = \mathbf{G}\boldsymbol{m}\,, \tag{1}$$

where $\boldsymbol{d}$ is an $N \times 1$ vector, $\boldsymbol{m}$ is an $M \times 1$ vector, and $\mathbf{G}$ is the $N \times M$ kernel matrix, which has been defined by *Last and Kubik (1983)*. In Eq. (1), $\boldsymbol{d}$ and $\mathbf{G}$ are known values that can be measured and calculated in advance, respectively; only $\boldsymbol{m}$ is unknown.

One solution to Eq. (1) can be formulated as an optimization form with a sequence of bound constraints using the interior-point algorithm, as described in the introduction, which can be expressed as follows:

$$\min \phi = \frac{1}{2}\phi_d + \frac{1}{2}\mu\phi_m - \lambda\phi_\lambda\,, \quad \text{subject to } \boldsymbol{m}_{min} \le \boldsymbol{m} \le \boldsymbol{m}_{max}\,, \tag{2}$$

where ϕ is the object function comprising the weighted sum of a data misfit, ϕ_d, the weighted sum of the model norm, ϕ_m, and the sum of a logarithmic barrier function that represents the specific mathematical expressions of the interior-point algorithm, ϕ_λ. The constant $1/2$ was applied to cancel the two values produced by the subsequent differentiation in Eq. (2), μ is the regularization parameter controlling the role of ϕ_m, and

λ has an analogous effect on controlling the role of ϕ_λ as a logarithmic barrier parameter. Here, $\boldsymbol{m}_{min}$ and $\boldsymbol{m}_{max}$ denote the lower- and upper-bound vectors, respectively, and ϕ_d is defined as follows:

$$\phi_d = \left\| \mathbf{W}_d \left(\mathbf{G}\boldsymbol{m} - \boldsymbol{d} \right) \right\|_2^2, \tag{3}$$

where $\mathbf{W}_d$ denotes the weight matrix of the gravity data, which is typically diagonal and emphasizes the different data performances with various errors in the inversion. Here, ϕ_m is defined as follows:

$$\phi_m = \left\| \mathbf{W}_m \left(\boldsymbol{m} - \boldsymbol{m}_{apr} \right) \right\|_2^2, \tag{4}$$

where $\boldsymbol{m}_{apr}$ is the reference model of the known prior information, which can be regarded as zero with all entries equal to zero and, thus, be removed from Eq. (4) when there is no prior known information. Furthermore, $\mathbf{W}_m$ is the weight matrix of the density model and is composed of the depth weight matrix, $\mathbf{W}_z$, the compactness weight matrix, $\mathbf{W}_c$, and the kernel weight matrix, $\mathbf{W}_a$. These three weight matrices are described later in this section.

The logarithmic barrier function that represents the specific mathematical expressions of the interior-point algorithm, ϕ_λ, is defined as follows:

$$\phi_\lambda = \sum_{j=1}^{n} \ln \left(\frac{\boldsymbol{m}_j - \boldsymbol{m}_{min} + \sigma^2}{\boldsymbol{m}_{max} - \boldsymbol{m}_{min}} \right) + \sum_{j=1}^{n} \ln \left(\frac{\boldsymbol{m}_{max} - \boldsymbol{m}_j + \sigma^2}{\boldsymbol{m}_{max} - \boldsymbol{m}_{min}} \right). \tag{5}$$

This functional of ϕ_λ, together with λ in Eq. (2), can effectively control the recovered values within the bounds. When $\boldsymbol{m}_j$ is far from the bounds, ϕ_λ has little effect on the objective function ϕ, which is mainly determined by ϕ_d and ϕ_m. As $\boldsymbol{m}_j$ gradually approaches the boundaries, ϕ_λ will gradually approach ∞. Equation (5) is slightly different from the one introduced by *Li et al. (2018)*, where an additional parameter σ (approximately 10^{-10}) is introduced to avoid zero value in the denominator after the differentiation of Eq. (5), when $\boldsymbol{m}_j$ equals the bound values of $\boldsymbol{m}_{min}$ or $\boldsymbol{m}_{max}$.

We obtained the specific form of Eq. (2), as illustrated by Eqs (3)–(5). To solve Eq. (2), the one-step Newton method is applied, as follows:

$$\Delta\boldsymbol{m} = -\frac{\phi'}{\phi''}. \tag{6}$$

According to the derivation of Eq. (3) at the n-th inner iteration of the k-th outer loop, we can obtain the following:

$$\left\{\mathbf{G}^{\mathrm{T}}\mathbf{W}_d^{\mathrm{T}}\mathbf{W}_d\mathbf{G}+\mu^{(k)}\left(\mathbf{W}_m^{(k)}\right)^{\mathrm{T}}\mathbf{W}_m^{(k)}+\lambda^{(n-1)}\left[\left(\mathbf{X}^{(n)}\right)^{-2}+\left(\mathbf{Y}^{(n)}\right)^{-2}\right]\right\}\Delta\boldsymbol{m}$$
$$=-\mathbf{G}^{\mathrm{T}}\mathbf{W}_d^{\mathrm{T}}\mathbf{W}_d\left(\mathbf{G}\boldsymbol{m}^{(n-1)}-\boldsymbol{d}\right)-\mu^{(k)}\left(\mathbf{W}_m^{(k)}\right)^{\mathrm{T}}\mathbf{W}_m^{(k)}\left(\boldsymbol{m}-\boldsymbol{m}_{apr}\right)^{(n-1)} \tag{7}$$
$$+\lambda^{(n-1)}\left[\left(\mathbf{X}^{(n)}\right)^{-1}+\left(\mathbf{Y}^{(n)}\right)^{-1}\right]\boldsymbol{e},$$

where

$$\mathbf{X}^{(n)}=\mathrm{diag}\left(\boldsymbol{m}^{(n-1)}-\boldsymbol{m}_{min}+\sigma^2\right),\quad \mathbf{Y}^{(n)}=\mathrm{diag}\left(\boldsymbol{m}^{(n-1)}-\boldsymbol{m}_{max}+\sigma^2\right). \tag{8}$$

We could consider $\boldsymbol{m}_{apr}$ as a zero vector of dimension M when it is unknown in practice. Next, λ is the barrier parameter, which is defined as follows:

$$\lambda=\frac{\phi_d+\phi_m}{\phi_\lambda}. \tag{9}$$

Finally, $\boldsymbol{e}$ is a vector of dimension M with all components equal to one.

In Eq. (7), each iteration contains an inner and outer loop, where $\Delta\boldsymbol{m}$ updates in the inner loop, leading to updates of λ, $\mathbf{X}$, and $\mathbf{Y}$ in the inner loop. The outer loop mainly updates $\mathbf{W}_m$ and μ. $\mathbf{W}_m$ is also decided by $\Delta\boldsymbol{m}$ from the inner loop while μ is obtained using the line-search method for synthetic data, with a known noise, or using the L-curve method for field data, with unknown noise. *Li et al. (2018)* and *Li and Oldenburg (2003)* have provide detailed descriptions of this process, including the definition of the initial value of μ, $\boldsymbol{m}$ and λ.

As it is highly time-consuming to directly solve Eq. (7) based on the matrix inversion, the preconditioned conjugate gradient method was applied to solve Eq. (7). After obtaining $\Delta\boldsymbol{m}$, the model $\boldsymbol{m}$ was updated with a gradually reduced step length in the inner loop. Thus, we obtained the following:

$$\boldsymbol{m}^{(n)}=\boldsymbol{m}^{(n-1)}+\gamma\varepsilon^{(n)}\Delta\boldsymbol{m}, \tag{10}$$

where $\gamma=0.925$ in this study (according to *Li and Oldenburg, 2003*) and $\varepsilon^{(n)}$ is a scalar determined by $\Delta\boldsymbol{m}$ as follows:

$$\varepsilon^{(n)}=\begin{cases}1 \quad \text{if} \quad \boldsymbol{m}_{max}>\boldsymbol{m}^{(n-1)}+\Delta\boldsymbol{m}>\boldsymbol{m}_{min}, \\ \min\left(\min\limits_{\Delta m_i<0}\dfrac{\boldsymbol{m}^{(n-1)}-\boldsymbol{m}_{min}}{|\Delta m_i|},\ \min\limits_{\Delta m_i>0}\dfrac{\boldsymbol{m}_{max}-\boldsymbol{m}^{(n-1)}}{|\Delta m_i|}\right) \text{otherwise}.\end{cases} \tag{11}$$

The criteria for terminating the iterations can be found in *Li et al. (2018)*.

The weighting matrix $\mathbf{W}_m$ is defined as follows:

$$\mathbf{W}_m = \mathbf{W}_z \mathbf{W}_c \mathbf{W}_a , \tag{12}$$

where $\mathbf{W}_z$ is a diagonal weighting matrix used to counteract the depth-dependent decay of the sensitivity matrix in the vertical direction, $\mathbf{W}_c$ is a diagonal weighting matrix that changes continuously as the iteration progresses, and $\mathbf{W}_a$ is a diagonal weighting matrix consisting of the elements of the kernel function matrix $\mathbf{G}$. The relative specific expressions for these variables are provided here for clarity. First, $\mathbf{W}_z$ and $\mathbf{W}_a$ for the j-th model are defined as follows (*Li and Oldenburg, 1996*; *Zhdanov, 2015*):

$$\mathbf{W}_z = \mathrm{diag}\left(z_j + z_0 \right)^{-\alpha} , \quad \mathbf{W}_a = \mathrm{diag} \sum_{j=1}^{M} \sum_{i=1}^{N} \left| G_{ij} \right|^{-1} , \tag{13}$$

where z_j is the depth of the j-th model, z_0 is the height of the observation point, α is a constant usually chosen to reproduce the exponential decay of gravity (*Williams, 2008*). Next, $\mathbf{W}_c$ can be defined as follows (*Last and Kubik, 1983*):

$$\mathbf{W}_c = \mathrm{diag} \left| m_j^{\beta} + \sigma^2 \right|^{-1} , \quad j = 1, 2, \ldots, m , \tag{14}$$

where β and σ are both constants; β is the compactness factor, which typically ranges from 0 to 2. The absolute value guarantees that $\mathbf{W}_c$ will always be a positive real matrix, because $m_j^{\beta} + \sigma^2$ is an imaginary number for $m_j < 0$ and $\beta > 0$ ($\beta \neq 2$). However, as shown by *Ghalehnoee et al. (2017)*, the solution is always fuzzy, which indicates that several recovered models do not reach the lower and upper bounds.

Finally, the nonzero values of the recovered model should be equal to the relative lower and upper bounds. Parameter β is the key factor that affects the sharpness of the recovered model. If β is not sufficiently large (usually $0 < \beta \leq 2$), the recovered model will be characterized by fuzzy boundaries in certain experiments. However, if β is too large, the recovered model will not be controlled within the designated boundaries after completing the final number of iterations when using the boundary constraint method described in *Ghalehnoee et al. (2017)*. That is why β is only equal to 1 in the third synthetic example reported in *Ghalehnoee et al. (2017)*. Thus, the inertia-point method is applied here, as expressed in Eq. (5), to allow for the use of a larger β while preventing the recovered model from violating the constraints.

Finally, to evaluate the merits of the recovered model, a relative L_2 norm was used to calculate the reconstruction error as follows:

$$re = \frac{\left\| \boldsymbol{m}_r - \boldsymbol{m}_t \right\|_2}{\left\| \boldsymbol{m}_t \right\|_2} , \tag{15}$$

where $\boldsymbol{m}_r$ is the recovered model and $\boldsymbol{m}_t$ is the true model.

3. RESULTS

3.1. Synthetic data inversion

We used three synthetic examples to test the validity of our proposed approach. In all three examples, the gravity anomaly data set was obtained by equidistant observations (5-m spacing) in the horizontal direction with or without Gaussian noise, a mean of zero, and a standard deviation of a certain proportion of the accurate data (10%). The corresponding model was constructed for the same square with a length of 5 m. The blue dashed rectangles indicate the locations of the true models. The lower and upper bounds were set to 0 and 1 g cm^{-3} for the first example, whereas they were defined as −1 and 1 g cm^{-3}, respectively, for both of the other examples. All examples were set to relatively more complex inversion models with a higher inversion depth compared with the method (Method 1) described in *Ghalehnoee et al. (2017)*.

The first example considers two density contrasts adjacent to each other at different depths. The corresponding gravity anomaly data free of noise (Fig. 1) were used to invert the model blocks, which are both 20 × 20 m, with a 10-m distance at depths of 45, 95, and 145 m. The left and right blocks, indicated by the dashed rectangles in Fig. 2, have density of 1 and 0.5 g cm^{-3}, respectively. The β values of the models recovered via Methods 1 and 2 were 2 and 2.1, respectively. As shown in Fig. 2a,b,c, the recovered models inverted by Method 1 are all connected whether at shallow, medium, or deep depths; however, the recovered models inverted by Method 2, as shown in Fig. 2d,e,f, are all separate. The latter is more in line with the actual situation.

The second example included two synthetic tests, both of which were composed of three separated bodies with one negative and two positive blocks distributed along the vertical direction. The first test was as follows: the left and middle models were both 70 × 20 m at a depth of 95 m and the right model was 30 × 30 m at a depth of 135 m. In addition, the synthetic gravity anomaly data were noise-free to allow further exploration of the validity of our method when positive and negative blocks existed at the same time in the inversion. The second test was as follows: the left and middle models were both 70 × 20 m at a depth of 95 m while the right model was 40 × 40 m at a depth of 155 m.

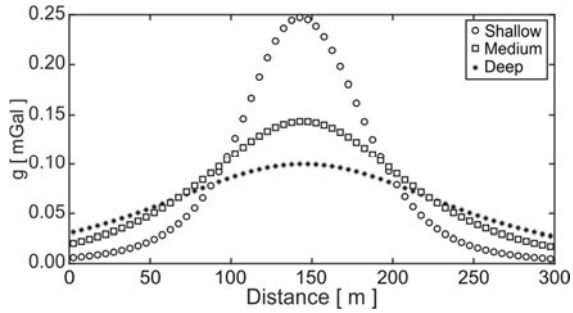

Fig. 1. Gravity acceleration *g* of anomaly produced by two model blocks at different depths (see Fig. 2). The observation points are located at 5-m equidistant intervals in the horizontal direction.

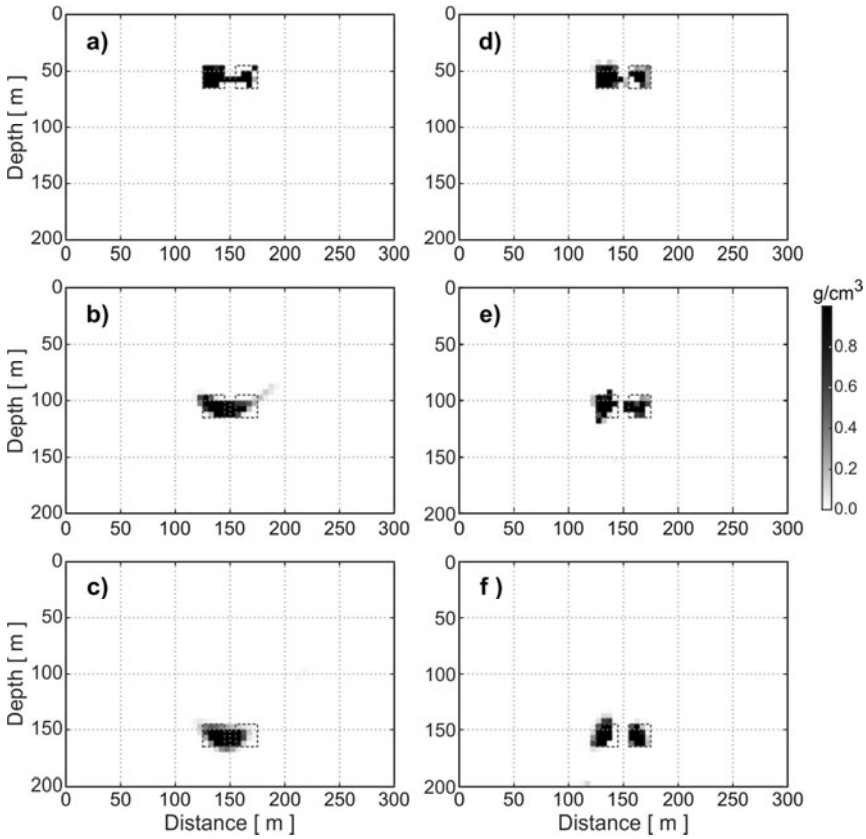

Fig. 2. Inversion results of the gravity anomaly data shown in Fig. 1, with Method 1 (**a, b, c**) and Method 2 (**d, e, f**). The dashed rectangles indicate the true positions of the blocks.

The data were contaminated by noise equivalent to 10% of the accurate datum. Figures 3 and 4 show the relative synthetic data and their misfit.

Figures 5 and 6 show that Method 2 can obtain sharper boundaries than Method 1. In the actual process, we observed that the compactness factor β can be set to no more than two. For $\beta > 2$ in Method 1, the inversion value cannot be constrained within the designated bounds of –1 and 1 g cm^{-3}. Moreover, the edge of the recovered model is not sufficiently sharp when $\beta = 2$, as shown in Figs 5a and 6a. However, with Method 2, β can be set to a slightly higher value of 2.1, which leads to a more accurate inversion solution, as shown in Figs 5b and 6b. According to Eq. (15), the reconstruction errors are 18.69% and 17.57% for the noise-free test using Methods 1 and 2, respectively, and 59.50% and 43.84% for the noise-contaminated test, respectively.

The third example was as follows: three bodies contained negative and positive values at a high depth, where the density bodies had certain inclinations. The gravity data were also contaminated by noise equivalent to 10% of the accurate datum. This example is

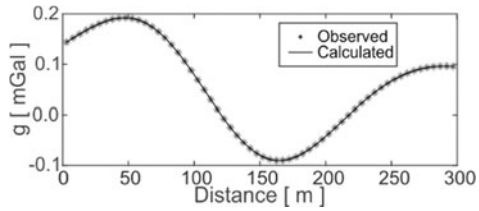

Fig. 3. Gravity acceleration g of anomaly without noise for the first test of the second synthetic example.

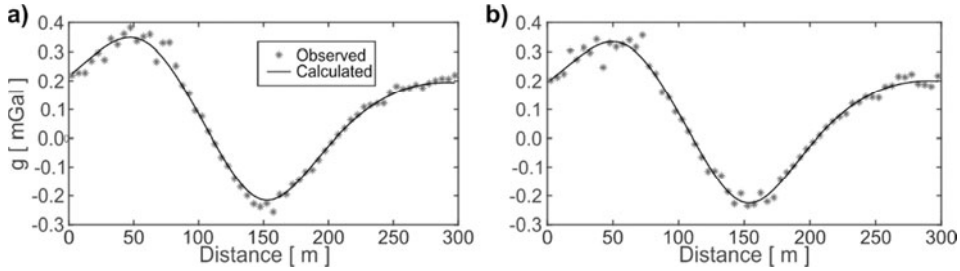

Fig. 4. Observed and calculated misfit of the gravity acceleration g of anomaly using **a)** Method 1, and **b)** Method 2 for the second test of the second synthetic example.

similar to a portion of one example in the 3-D case used in *Li and Oldenburg (1998)*. Figure 7b displays the inversion solution obtained with Method 1, which has a reconstruction error of 110.00% and compactness factor β of 1.0. Figure 7d shows the results for Method 2, with a reconstruction error of 78.86% and $\beta = 1.1$. The two recovered models at the left obtained with Method 1 connect with each other with obscure boundaries while the inversion solution with Method 2 has sharper boundaries. Figure 7a,c shows the relative data misfits.

Figure 8 shows the reconstruction errors in the two methods, based on Eq. (15), as present in the three examples. It shows that there are no marked differences between Method 1 and 2 when the gravity data are not contaminated with Gaussian noise. The maximum difference in the two methods does not exceed 4%; this appears in the inversion of the contrasts in density located at the shallow depth in the first example. When the gravity data is contaminated, the differences in the reconstruction errors between the two methods is significant; the minimum difference is 15.66% in the second synthetic tests of the second example and the maximum is 31.14% in the third example.

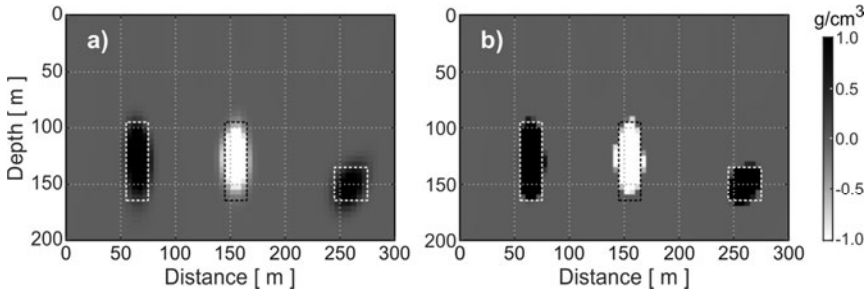

Fig. 5. Inversion results of the gravity anomaly data shown in Fig. 3 with **a)** Method 1, and **b)** Method 2 for the first test of the second synthetic example. The dashed rectangles indicate the true positions of the blocks. The exponential compactness factor β has values of 2 (a) and 2.1 (b).

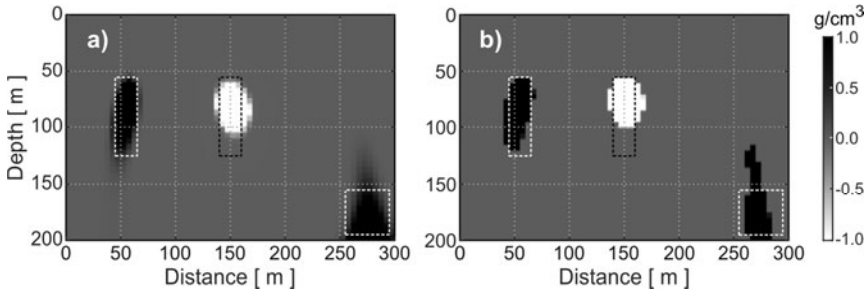

Fig. 6. Inversion results for three blocks obtained with **a)** Method 1, and **b)** Method 2 for the second test of the second synthetic example. The exponential compactness factor β has values of 2 (a) and 2.1 (b). The dashed rectangles indicate the true positions of the blocks.

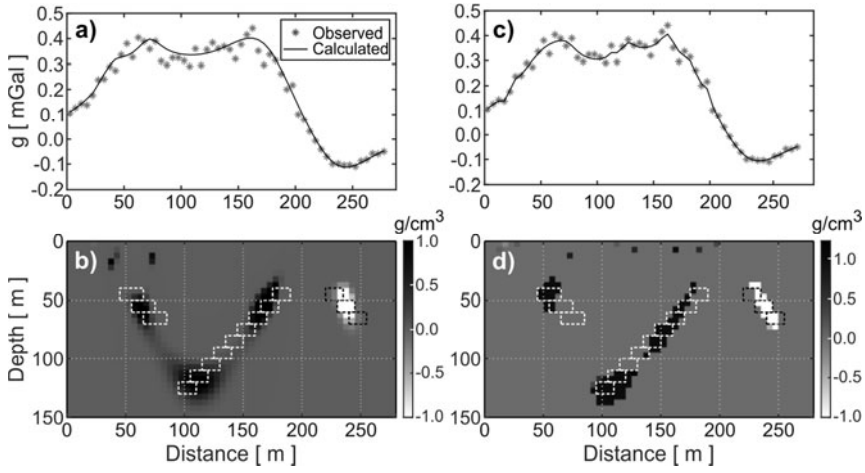

Fig. 7. **a)** Gravity acceleration g misfit and **b)** inversion results of the third synthetic example obtained with Method 1, **c)** and **d)** the same for Method 2. The compactness factor is equal to 1.0 and 1.1, respectively. The dashed rectangles in b) and d) indicate the true positions of the blocks.

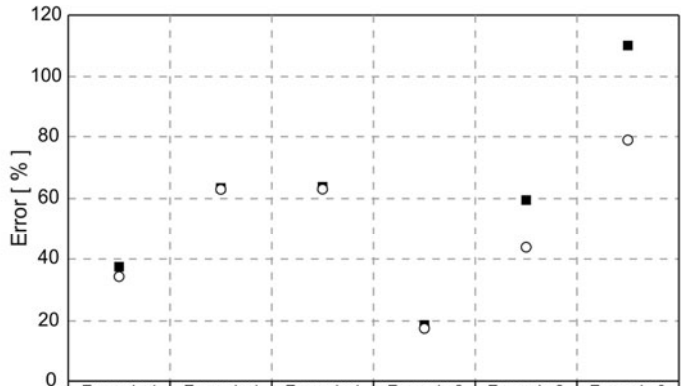

	Example 1 (Fig. 2a,d)	Example 1 (Fig. 2b,e)	Example 1 (Fig. 2c,f)	Example 2 (Fig. 5)	Example 2 (Fig. 6)	Example 3 (Fig. 7)
■ Method 1	37.45	63.45	63.86	18.69	59.50	110.00
○ Method 2	34.25	63.00	63.10	17.57	43.84	78.86

Fig. 8. Comparison of the reconstruction errors of Method 1 and Method 2, based on Eq. (15), in three synthetic examples.

3.2. Field data inversion

The two methods were also compared using three sets of real gravity data. The first example in Fig. 9 shows the Bouguer anomaly along a profile over the Woodlawn massive sulfide ore body, New South Wales, Australia (*Templeton, 1981*; *Ghalehnoee et al., 2017*). The Woodlawn ore body is geologically classified as a stratiform volcanogenic copper-lead-zinc deposit that occurs within acidic volcanic host rocks. The average densities of the massive sulfide ore and host rocks are approximately 3.9 and 2.9 g cm^{-3}, respectively, which indicates that the target density contrast is 1 g cm^{-3}. The model was designed for unit square of 5 × 5 m. As the observation error is unknown, we assumed that the data had minimal errors and, therefore, employed a small regularization parameter in the initial inversion process.

The calculations of the gravity anomaly with the two methods are both similar to the observed gravity anomaly, as shown in Fig. 10a,b. However, the recovered model in Fig. 10c obtained with Method 1 has obscure boundaries with a compactness factor equal to two, whereas the recovered model obtained with Model 2, with $\beta = 2.1$, is characterized by sharp boundaries, as shown in Fig. 10d. Nevertheless, the disadvantage of Method 2 is the appearance of more false density contrasts in the shallow layer with the value of the upper boundary (1 g cm^{-3}) than in Method 1. This problem is likely caused by observation noise, which appears to have a more significant effect in the shallow layer.

The second field test shown in Fig. 11 was the inversion of the Northwest Ore Body at Iron Mountain Mine, Missouri (*Barbosa and Silva, 1994*). The presence of this regional component was inferred from geological information on the existence of large regional features associated with iron mineralization (*Hansen et al., 1966*). Two ore bodies remained beneath the surface in the inversion area after the regional anomaly was removed by *Barbosa and Silva (1994)*. The inversion region contains 60 × 30 blocks in

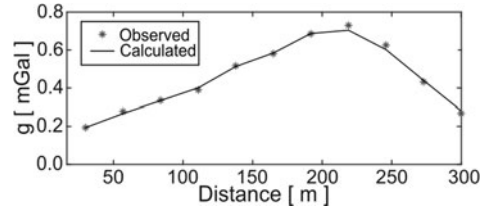

Fig. 9. Measured gravity acceleration g of Bouguer anomaly along a profile over the Woodlawn massive sulfide ore body, New South Wales, Australia, and calculated results of *Ghalehnoee et al. (2017)*.

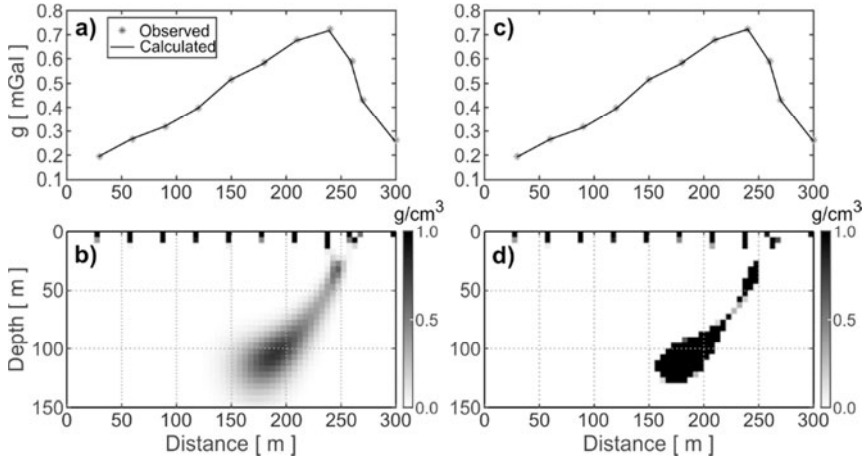

Fig. 10. Misfit and inversion results of the gravity acceleration g of Bouguer anomaly along a profile over the Woodlawn massive sulfide ore body, New South Wales, Australia (shown in Fig. 9), obtained with Method 1 (**a** and **b**) and Method 2 (**c** and **d**), with the compactness factors $\beta = 2.0$ and 2.1, respectively.

total, with each model unit having a size of 5 × 5 m. As in the first field test, the target density contrast was 1 g cm^{-3}. The lower and upper limits were defined as 0 and 0.1 g cm^{-3} to constrain the density inversion result. Figure 12a,c illustrates the misfit between the observation data and calculation results obtained with the two constrained methods. We also initially applied a small regularization parameter, μ, in the inversion process. Figure 12b,d shows the inversion results for the two methods. The inversion with Method 2, with a higher compactness factor ($\beta = 2.1$), yielded sharper recovered boundaries than Method 1 with $\beta = 2.0$. Although the inversion with the interior-point method has sharper boundaries, the locations of the right ore body in the inversion results with both methods in Fig. 12b,d are not sufficiently accurate compared to the true ore body distribution along the vertical direction, which indicates that more prior information should be considered when inverting highly complex ore bodies.

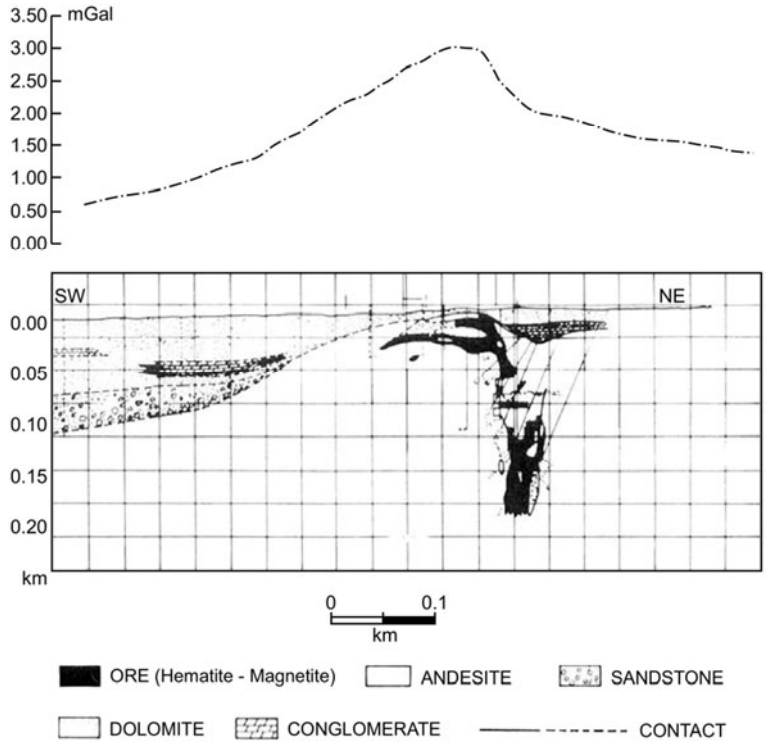

Fig. 11. Top: Bouguer anomaly gravity *g* profile, **Bottom:** corresponding geological cross-section of the Northwest ore body at the Iron Mountain Mine, Missouri (*Hansen et al., 1966*, © Society of Exploration Geophysicists).

The third example shown in Fig. 13 represents three ore bodies under the surface in a larger area (*Silva and Barbosa, 2006*). The gravity profile (solid curve) across a Greenstone belt consists of metavolcanic sedimentary rocks in the Rio Maria region of the state of Para, Brazil, where the observation data (dashed curve) were fitted by *Souza et al. (1992)* in Fig. 13a. The density contrast between the metavolcanic sedimentary and granitoid rocks was approximately 0.3 g cm^{-3} based on rock samples collected from the outcrops. According to *Silva and Barbosa (2006)*, gravity sources A, B, and C have uniform density contrasts of 0.3, 0.32, and 0.32 g cm^{-3}, respectively, as shown in Fig. 13b. Figure 14b shows the inversion results using Method 1, with a compactness factor $\beta = 1.0$. Figure 14d shows the results using Method 2 with a compactness factor $\beta = 1.1$, which has sharper boundaries than the results using Method 1. At the same time, we were not able to accurately obtain the actual ore body. In this field test, a high value of β cannot be used even with the interior-point constraint method. A similar situation can be observed in the third synthetic example reported in *Ghalehnoee et al. (2017)*, where β is equal to one. This may suggest that β cannot be excessively high when the data contain severe errors and the models are complex.

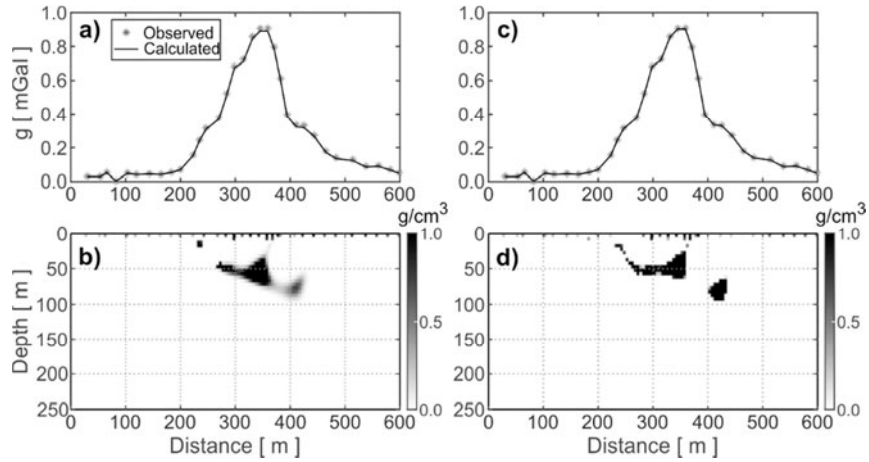

Fig. 12. Misfit of the gravity acceleration g of the Bouguer anomaly and inversion results from the Northwest Ore Body at the Iron Mountain Mine, Missouri (shown in Fig. 11), with Method 1 (**a** and **b**) and Method 2 (**c** and **d**), with the compactness factors $\beta = 2.0$ and 2.1, respectively.

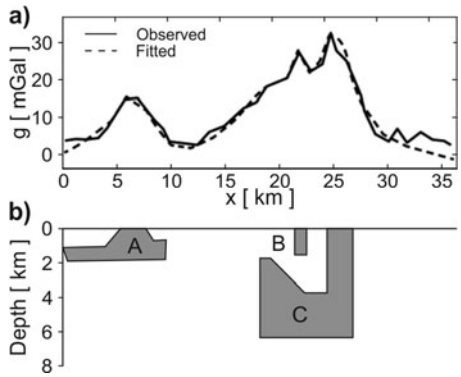

Fig. 13. **a)** Bouguer gravity g profile, and **b)** geological cross-section of the Rio Maria region in the state of Para, Brazil (re-drawn after *Souza et al., 1992*).

4. CONCLUSIONS

In this study, we optimized the gravity sparse inversion process by minimizing the total objective function subject to boundary constraints handled by an interior-point method. The proposed model weighting function integrates the depth weighting, compact weighting, and kernel weighting functions into the inversion process. A recovered model with sharper boundaries was obtained using a higher value of the compactness factor β on the premise that the values of the recovered model cannot exceed the upper and lower bounds pre-specified during the inversion process. The inversion model can be either

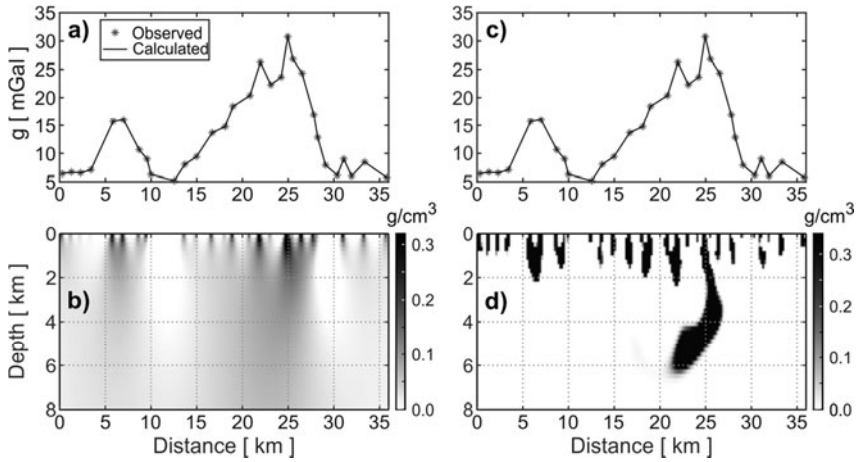

Fig. 14. Misfit of the gravity acceleration g of the Bouguer anomaly and inversion results from the Rio Maria region in the state of Para, Brazil (shown in Fig. 13), with Method 1 (**a** and **b**) and Method 2 (**c** and **d**), with the compactness factor $\beta = 1.0$ and 1.1, respectively.

positive or negative. However, when a practical ore body is relatively complex or the observation error is severe, the compactness factor cannot be excessively high, even when using the interior-point method. In addition, we found that, to improve the accuracy of the inversion results, factors, such as underground drilling information, should be considered in addition to upper and lower boundary constraint information.

Acknowledgements: This study was funded by the National Key R&D Program of China (Grants Nos 2018YFC1503606 and 2017YFC1500501); the Science and Technology Basic Work (Grant No. 2015FY210400); the Earthquake Industry Research Project (Grant No. 201508009) funded by the Ministry of Science and Technology of the People's Republic of China; the National Natural Science Foundation of China (Grant No. 41804010); and the Natural Science Foundation of Tianjin (Grant No. 17JCYBJC21600). We would like to thank Prof. Z.L. Li of Hebei University of Engineering and Prof. S. Chen of the Institute of Geophysics, China Earthquake Administration, for providing detailed guidance. We sincerely appreciate the rigorous and careful work of the editor Christian Voigt and two reviewers, who have helped to improve the paper significantly and encourage and guide our future research.

References

Barbosa V.C.F. and Silva J.B.C., 1994. Generalized compact gravity inversion. *Geophysics*, **59**, 57–68.

Blakely R.J., 1995. *Potential Theory in Gravity and Magnetic Applications*. Cambridge University Press, Cambridge, U.K.

Chen S., Zhang J. and Shi Y.L., 2008. Gravity inversion using the frequency characteristics of the density distribution. *Appl. Geophys.*, **5(2)**, 99–106.

Ghalehnoee M.H., Ansari A. and Ghorbani A., 2017. Improving compact gravity inversion using new weighting functions. *Geophys. J. Int.*, **28**, 546–560.

Guillen A. and Menichetti V., 1984. Gravity and magnetic inversion with minimization of a specific functional. *Geophysics*, **49**, 1354–1360.

Hadamard J., 1902. Sur les problèmes aux derivées partielles et leur signification physique. *Princeton Univ. Bull.*, **13**, 49–52 (in French).

Hansen P.C., 1994. Regularization tools: A Matlab package for analysis and solution of discrete ill-posed problems. *Numer. Algorithms*, **6**, 1–35.

Hansen P.C. and O'Leary D.P., 1993. The use of the L-curve in the regularization of discrete ill-posed problems. *SIAM J. Sci. Comput.ing*, **14**, 1487–1503.

Hansen D.A., Gross W.H., Strangway D.W., Webb J.E., Leney G.W., Riddell P.A., Parker Gay S. Jr., Hinze W.J. and Zablocki C.J., 1966. The search for iron ore. In: Hansen D.A., Heinrichs W.E. Jr., Holmer R.C., MacDougall R.E., Rogers G.R., Sumner J.S. and Ward S.H. (Eds), *Mining Geophysics, Volume 1: Case Histories*. Society of Exploration Geophysicists, Tulsa, OK, 357–492.

Last B.J. and Kubik K., 1983. Compact gravity inversion. *Geophysics*, **34**, 65–74.

Li Y.G. and Oldenburg D.W., 1996. 3-D inversion of magnetic data. *Geophysics*, **61**, 394–408.

Li Y.G. and Oldenburg D.W., 1998. 3-D inversion of gravity data. *Geophysics*, **63**, 109–119.

Li Y.G. and Oldenburg D.W., 2003. Fast inversion of large-scale magnetic data using wavelet transforms and a logarithmic barrier method. *Geophys. J. Int.*, **152**, 251–265.

Li Z.L., Yao C.L., Zheng Y.M., Wang J.H. and Zhang Y.W., 2018. 3-D magnetic sparse inversion using an interior-point method. *Geophysics*, **83**, J15–J32.

Mendonca C.A. and Silva J.B.C., 1994. The equivalent data concept applied to the interpolation of potential field data. *Geophysics*, **59**, 722–732.

Mendonca C.A. and Silva J.B.C., 1995. Interpolation of potential field data by equivalent layer and minimum curvature: A comparative analysis. *Geophysics*, **60**, 399–407.

Pilkington M., 1997. 3-D magnetic imaging using conjugate gradients. *Geophysics*, **62**, 1132–1142.

Pilkington M., 2009. 3-D magnetic data-space inversion with sparseness constraints. *Geophysics*, **74**, L7–L15.

Portniaguine O. and Zhdanov M.S., 1999. Focusing geophysical inversion images. *Geophysics*, **64**, 874–887.

Rosas-Carbajal M., Jourde K., Marteau J., Deroussi S., Komorowski J.C. and Gibert D., 2017. Three-dimensional density structure of La Soufrière de Guadeloupe lava dome from simultaneous muon radiographies and gravity data. *Geophys. Res. Lett.*, **44**, 6743–6751.

Silva J.B.C. and Barbosa V.C.F., 2006. Interactive gravity inversion. *Geophysics*, **71**, J1–J9.

Souza Z.S., Luiz J.G., Cruz J.C.R. and Paiva R.N., 1992. Geometria de greenstone belts Arqueanos da região de Rio Maria (sudeste do Pará, Brasil), a partir de interpretação gravimétrica (Geometry of Archaean greenstone belts from Rio Maria (SW Pará province, Brazil)). *Revista Brasileira de Geociências*, **22**, 198–203 (in Portuguese).

Stocco S., Godio A. and Sambuelli L., 2009. Modelling and compact inversion of magnetic data. *Comput. Geosci.*, **35**, 2111–2118.

Sun J. and Li Y., 2014. Adaptive Lp inversion for simultaneous recovery of both blocky and smooth features in geophysical model. *Geophys. J. Int*, **197**, 882–899.

Templeton R.J., 1981. Gravity surveys at Woodlawn. In: Whiteley R.J. (Ed.), *Geophysical Case Study of the Woodlawn Ore Body, New South Wales, Australia*. Pergamon Press, New York, 485–494.

Tikhonov A.N. and Arsenin V.Y., 1977. *Solution of Ill-Posed Problems*. W.H. Winston & Sons, New York.

Tikhonov A.N., 1943. On the stability of inverse problems. *Doklady AN SSSR*, **39**, 195−198 (in Russian).

Williams N.C., 2008. *Geologically-Constrained UBC-GIF Gravity and Magnetic Inversion with Examples from the Agnew-Wiluna Greenstone Belt, Western Australia*. PhD Thesis. The University of British Columbia, Vancouver, Canada.

Zhdanov M.S., 2015. *Inverse Theory and Applications in Geophysics*. Elsevier, Amsterdam, The Netherlands.